

THREE DIMENSIONAL IMAGING IN THE POSITRON CAMERA
USING FOURIER TECHNIQUES

Gilbert Chu

Stanford Linear Accelerator Center
Stanford University, Stanford, California 94305

and

Kwok-Cheong Tam

Lawrence Berkeley Laboratory
Berkeley, California 94720

ABSTRACT

A mathematical algorithm for three dimensional reconstructions in the positron camera is described. Fourier techniques have been adapted for use in analyzing the data from cameras with limited detector configuration. Noise instabilities from random fluctuations in the data are discussed and treated. The technique is tested on a computer generated phantom and the results are presented. There is a discussion of how the effects of Compton scattering and detector response may be incorporated into the algorithm. On the basis of these investigations, it is concluded that the method is feasible and practical for obtaining accurate reconstructions.

(Submitted to Physics in Medicine and Biology.)

*Work supported by the Energy Research and Development Administration.

I. Introduction

The use of radioactive tracers for diagnosis in medicine has enjoyed a long history. Radioactive isotopes which undergo positron beta decay seem to be an especially effective probe for detecting and locating medical disorders.

Typically, the radioisotope is injected into the patient's blood stream, and then allowed to assume a quasi-equilibrium distribution in the tissue. A nucleus of the tracer can emit a low energy positron. (The energy maximum for commonly used tracers is usually 1-3 MeV.) The positron passes through the tissue, eventually coming to rest and annihilating with an electron, producing two photons, which emerge back-to-back in the center-of-mass frame, each with an energy of about 0.51 MeV:



Positrons with an energy of 1 MeV, in tissue of typical densities, will usually annihilate within 1 mm of the point of emission and the photons will be anti-parallel to within 10 milliradians (1).

The photons may then escape from the patient's body and fall onto a detector, commonly known as a positron camera. If the camera detects two photons in coincidence, then it may be inferred that a positron was emitted somewhere along the straight line defined by the detector loci.

A number of positron cameras have been conceived and built. There are systems using arrays of sodium iodide crystals (2,3,4), using multiwire proportional chambers with lead converters (5,6), and using multiwire proportional chambers with liquid Xenon (7). Therefore, the positron camera has been shown to be a feasible tool for medical diagnosis. A schematic diagram of a possible detector configuration is shown in Fig. 1. The camera is being used to image the radioisotope density distribution in a hypothetical phantom's head.

For the purposes of this paper we shall assume that for each electron-positron annihilation event in Eq. (1. 1) the two photons are antiparallel and are produced at the location of the emitter. Therefore, the data may be thought of as a set of straight lines imbedded in three space. For any given event, the exact location of the emitter along the line cannot be determined, modulo the constraint that it be somewhere inside the patient's body.

The great value of the positron camera lies in the fact that it is capable of measuring the density distribution of the tracer in three dimensions. For example, a brain tumor may absorb the radioisotope at a much greater rate than the surrounding tissue, and a positron camera could then determine the exact location of the tumor. Unfortunately the data gathered by such imaging devices does not correspond in a straightforward way to the density distribution. Metaphorically, the camera is capable of photographing a patient's internal organs, but the picture must be developed. Some mathematical analysis must be performed on the data before the density distribution can be specified.

There is a rapidly growing literature on the mathematical techniques for three dimensional reconstructions (8). There are a number of methods which may be applied to the particular case of the positron camera. Perhaps the simplest method is the technique of back projection. The volume to be studied is imagined to be divided into a series of parallel planes. Each event corresponds to a straight line, and the intersection points of that line with each of the planes is computed. The distribution of intersection points in each plane defines the back projection. An adaptation of this technique has already been used to show pictures obtained from human patients (6). Although back projection is simple, it is not an attempt to obtain the true solution for the density distribution. A tumor in one plane will always cast a shadow on all other planes, and,

conversely, background from all planes will cast shadows on the tumor planes. Thus variations in tracer density tend to be washed out. More sophisticated methods may be employed which are capable of finding the true solution and removing the shadow effect. In this paper we shall describe an algorithm for three dimensional reconstruction using Fourier techniques (9), and report on our results when the technique is applied to a computer generated phantom.

Section II describes how the data may be used to compute a scalar field for the radioisotope distribution. Section III describes the mathematical problem in terms of the scalar field and shows a solution to the problem in terms of continuous Fourier transforms. Section IV discusses how to implement the solution for the computer by using discrete Fourier transforms on a lattice. Section V shows how noise in the data leads to instabilities in the solution, and Section VI describes a method for removing the instabilities. Section VII summarizes the algorithm. Section VIII discusses the results of our methods when applied to a computer generated phantom. Section IX suggests a method for treating Compton scattering in the data.

II. A Point Emitter Generates a Scalar Field

Consider the idealized situation of a point emitter. The emitter will generate a set of straight lines passing through the origin, each of which is randomly oriented in three space. In the limit where the number of straight lines becomes large, it is possible to define an associated scalar field which is a function only of position relative to the point emitter. Thus an emitter located at \vec{r}_0 generates a scalar field $\phi_0(\vec{r} - \vec{r}_0)$.

In fact, the scalar field can assume any one of a large number of forms. We shall give a number of examples.

Example A.

Take a volume element located a distance $|\vec{r}-\vec{r}_0|$ from the emitter, subtending a solid angle $\delta\Omega$, with thickness δr . (See Fig. 2a.) The volume is:

$$\delta V = |\vec{r}-\vec{r}_0|^2 \delta r \delta\Omega$$

The probability that one of the lines generated by the emitter will pass through the volume element is $\delta\Omega/2\pi$. The line falls inside the volume element along a segment of length δr . Define a scalar field $\phi_0(\vec{r}-\vec{r}_0)$ associated with the point emitter as the mean line length per unit volume per event for randomly oriented lines emanating from \vec{r}_0 which pass through a volume element located at \vec{r} . Then, in the far field limit, $|\vec{r}-\vec{r}_0| \gg \delta r$,

$$\phi_0(\vec{r}-\vec{r}_0) \cong \frac{1}{2\pi |\vec{r}-\vec{r}_0|^2} \quad (2.1)$$

For a volume element of radius δr located at \vec{r}_0 , the scalar field can be easily calculated (see Fig. 2b):

$$\phi_0(\vec{0}) = \frac{3}{2\pi} \frac{1}{(\delta r)^2}$$

Thus, the scalar field is nonsingular for a finite volume element, but depends strongly on the size of the volume element. An accurate parametrization is given by

$$\phi_0(\vec{r}-\vec{r}_0) = \frac{1}{2\pi} \frac{1}{|\vec{r}-\vec{r}_0|^2 + a^2} \quad (2.2)$$

where $a = \delta r / \sqrt{3}$. Notice that as the dimension of the volume element vanishes, $a \rightarrow 0$, the scalar field assumes the asymptotic form of Eq. (2.1).

Example B.

Take an area element of area δA oriented perpendicular to the z-axis, at a distance $|\vec{r}-\vec{r}_0|$ from the emitter. (See Fig. 3.) The probability that one of

the lines will pass through the area element is

$$\frac{\delta A \cos \theta}{2\pi |\vec{r} - \vec{r}_0|^2}$$

in the limit where $|\vec{r} - \vec{r}_0|$ is much larger than the dimension of the area element, a . Here we can define the scalar field $\phi(\vec{r} - \vec{r}_0)$ as the average number of lines per unit area per event for lines emitted from \vec{r}_0 which pass through the oriented area element located at \vec{r} . In the far field limit, $|\vec{r} - \vec{r}_0| \gg a$,

$$\phi_0(\vec{r} - \vec{r}_0) \cong \frac{\cos \theta}{2\pi |\vec{r} - \vec{r}_0|^2} = \frac{(\vec{r} - \vec{r}_0) \cdot \hat{z}}{2\pi |\vec{r} - \vec{r}_0|^3} \quad (2.3)$$

For an area element located at \vec{r}_0 ,

$$\phi_0(\vec{0}) = \frac{1}{a^2}$$

Thus an accurate parametrization is given by

$$\phi_0(\vec{r} - \vec{r}_0) = \frac{1}{2\pi |\vec{r} - \vec{r}_0|^2 / \cos \theta + a^2} \quad (2.4)$$

As the dimension of the area element vanishes, $a \rightarrow 0$, the scalar field assumes the asymptotic form of Eq. (2.3).

Example C.

It is possible now to construct an entire class of scalar fields. Define $\phi_0(\vec{r} - \vec{r}_0)$ as the scalar field computed in Example B multiplied by $\cos^n \theta$, for any integer n . For $|\vec{r} - \vec{r}_0| \gg a$,

$$\phi_0(\vec{r} - \vec{r}_0) \cong \frac{\cos^{n+1} \theta}{2\pi |\vec{r} - \vec{r}_0|^2} \quad (2.5)$$

An accurate parametrization is given by

$$\phi_0(\vec{r} - \vec{r}_0) = \frac{\cos^n \theta}{2\pi |\vec{r} - \vec{r}_0|^2 / \cos \theta + a^2} \quad (2.6)$$

Thus, we have seen that a point emitter can generate a number of scalar fields using appropriate definitions for how it is to be measured. Each scalar field is a function only of position relative to the point emitter, and independent of the position of the emitter itself. The spectrum of possibilities provides us with the luxury of choosing the particular scalar field which will optimize our reconstructions. Each example in this section illustrates a legitimate scalar field, but there may be advantages in choosing one over the others. Example A, which requires the integrated line length passing through a cube, is more difficult to compute than Examples B or C, which only measure the intersection of a line with a unit area. In Example C, different choices of the integer n correspond to a large range of possible shapes for the scalar field, some of which are much more sharply peaked than others. In Example C, the scalar fields all possess a singularity (either a zero or a pole depending on n) at $\theta = \pi/2$.

III. The Reconstruction Problem is a Convolution

Suppose we have chosen some definition for how the scalar field ϕ_0 from a point emitter is to be measured. Then, an arbitrary distribution of radioisotope described by a density ρ will generate a scalar field ϕ given by the convolution,

$$\phi(\vec{r}) = \int d^3r' \phi_0(\vec{r} - \vec{r}') \rho(\vec{r}') \quad (3.1)$$

The field ϕ_0 appears as the Green's function or transfer function for the integral equation. If there are enough events to provide good statistics, the data from the positron camera measures the field ϕ . The problem is to solve Eq. (3.1) for the density distribution ρ , where both ϕ and ϕ_0 are known.

Any physically realizable density is integrable, and for an appropriately chosen definition, both ϕ_0 and ϕ are also integrable. Therefore, we may take

the Fourier transform of both sides of Eq. (3.1):

$$\Phi(\vec{p}) = R(\vec{p}) \Phi_0(\vec{p}) \quad (3.2)$$

where Φ , Φ_0 , and R are the Fourier transforms of ϕ , ϕ_0 , and ρ respectively.

The transform is defined as

$$\Phi(\vec{p}) = \int d^3r \phi(\vec{r}) \exp(2\pi i \vec{p} \cdot \vec{r}) \quad (3.3)$$

The solution of the problem is now very simple in momentum space

$$R(\vec{p}) = \Phi(\vec{p}) / \Phi_0(\vec{p}) \quad (3.4)$$

The density distribution in configuration space can then be obtained by taking the inverse transform,

$$\rho(\vec{r}) = \int d^3p R(\vec{p}) \exp(-2\pi i \vec{p} \cdot \vec{r}) \quad (3.5)$$

Thus, the solution of the problem in its simplest form is quite straightforward, once it can be expressed as a convolution integral equation.

However, the problem is never this simple in practice. Note that the convolution integral in Eq. (3.1) is to be performed over all space. Therefore, a major complication arises if the detection apparatus does not subtend the full 4π radians of solid angle. For example, the detector may lie in two parallel planes on each side of the patient's head as in Fig. 1. There will be no record of those events for which either of the two photons does not intersect the detector. Thus the scalar fields as described in Section II cannot be determined in a large region of space.

There is an elegant way to circumvent this difficulty by simply redefining the scalar fields. Usually the region to be scanned is characterizable by well defined boundaries. In a brain scan, the observed radioisotope density distribution may be confined to the head area by arranging lead shielding to absorb any photons which originate below the patient's neck. If the detectors are large

enough to extend beyond the boundaries of the head, then for each point \vec{r} in the head there is a "local cone of detection". Those back-to-back photons originating from \vec{r} which fall within the local cone will be detected. Those which fall outside the local cone will not be detected. The size of the local cone of detection is clearly a function of position \vec{r} . Define the "universal cone of detection" to be the smallest local cone of detection for all the points \vec{r} in the head. Any photons emitted within the universal cone will be detected, and the size of the universal cone is obviously independent of position.

A schematic illustration is given by Fig. 4. The universal cones for the points \vec{r}_1 and \vec{r}_2 are indicated by the shaded areas. At point \vec{r}_2 the local cone is significantly larger than the universal cone, and the boundaries of the local cone are shown. At point \vec{r}_1 the universal and local cones are identical.

Redefine the scalar field as follows. Consider only those events which fall within the universal cone. For the present, we shall disregard all the other events, which may in fact include a substantial fraction of the total number of events recorded by the detector. The scalar field is computed by any of the methods described in Section II, except that only those events which fall within the universal cone are used. The convolution equation will still hold,

$$\phi(\vec{r}) = \int d^3r' \phi_0(\vec{r}-\vec{r}')\rho(\vec{r}')$$

Here, the Green's function ϕ_0 is the scalar field of a point emitter restricted to the universal cone.

Notice that if the detector consists of two parallel plates, for example, then the scalar field will vanish for large regions of configuration space. Define a polar coordinate system in which the z-axis is perpendicular to the plane of the detectors and passes through their center. The angle θ is the angle between a

line and the z-axis. Then, the poles in the scalar fields described in Example C (for $n < 0$) will never appear since there can be no events oriented with $\theta = \pi/2$.

IV. Computation is Done on a Lattice

Obviously, any numerical reconstruction of the density distribution of radioisotope must be done by dividing space into a lattice of discrete points and then using discrete Fourier transforms to obtain the solution. The continuous integrals of Section III must be replaced by series representations with some finite cutoff.

Divide the region of space in the vicinity of the density distribution into a three dimensional lattice, N_x by N_y by N_z , with spacing between the lattice sites, $\delta_x, \delta_y, \delta_z$.

The scalar field can be computed by placing a volume element or an area element at each of the lattice sites and then using any of the methods described in Section II.

The discrete Fourier transform Φ of the field ϕ is expressed as a finite series,

$$\Phi(\vec{p}) = V \sum_{m_i=0}^{N_i-1} \phi(\vec{r}) \exp(2\pi i \vec{p} \cdot \vec{r}) \quad (4.1)$$

where the cell volume $V = \delta_x \delta_y \delta_z$ and the variables are placed on the lattice,

$$\vec{p} = \left(\frac{n_x}{N_x \delta_x}, \frac{n_y}{N_y \delta_y}, \frac{n_z}{N_z \delta_z} \right), \quad n_i=0, N_i-1 \quad (4.2)$$

$$\vec{r} = (m_x \delta_x, m_y \delta_y, m_z \delta_z)$$

The inverse transform is

$$\phi(\vec{r}) = \frac{1}{NV} \sum_{n_i=0}^{N_i-1} \Phi(\vec{p}) \exp(-2\pi i \vec{p} \cdot \vec{r}) \quad (4.3)$$

where $N = N_x N_y N_z$. Of course, Φ and ϕ are now both periodic, repeating in each dimension after each N_i lattice sites.

The lattice spacing is determined chiefly by four considerations: (a) the resolution desired for the reconstruction, (b) the need to minimize "aliasing" (10) in the Fourier transform, (c) the detector configuration, and (d) noise problems arising from the fact that only a finite number of events are detected. The problem of noise shall be addressed in the next section.

In (a), it is clear that the lattice spacing must be smaller than the desired resolution for the reconstruction.

In (b), aliasing is completely eliminated if the lattice spacings δ_i satisfy the relations,

$$\frac{1}{2\delta_i} \geq p(\max), \quad i = x, y, z \quad (4.4)$$

where $p(\max)$ are the magnitude of the largest momentum for which $\Phi(\vec{p})$ is non-vanishing. If the conditions (4.4) are not satisfied, then portions of $\Phi(\vec{p})$ from adjacent periods will begin to interfere with each other, resulting in what is known as aliasing. In practice, it may be the case that $\Phi(\vec{p})$ does not have a limiting momentum, and the best that can be done is to choose the lattice spacing small enough to minimize the effects of aliasing.

We have found that (c) the detector configuration is an important consideration in adjusting the relative size of the lattice in different dimensions. The ratio of lattice spacings $\delta_x : \delta_y : \delta_z$ should be chosen to minimize the effect of edge effects at the boundaries of the universal cone. Clearly, edge effects become less important as the lattice spacings are made smaller. But for a given size for the unit cell in the lattice, the optimum choice for the ratio of lattice spacings would be that for which the boundaries of the universal cone are closely

approximated by major diagonal planes in the lattice. In the two dimensional example of Fig. 4, the optimal choice would be

$$\delta_y/\delta_x = \tan (\theta/2) \quad (4.5)$$

where θ is the opening angle in the universal cone.

Once the lattice spacing is fixed, the size of the array is determined by choices for N_x , N_y , N_z . The array dimensions are given by

$$\Delta_i = N_i \delta_i \quad (4.6)$$

For a periodic function, if Δ_i are chosen equal to the period of the function, then the discrete Fourier transform will be free of "leakage" (10). However, the field ϕ is of noncompact support and manifestly aperiodic. Leakage must occur. The problem may be minimized by choosing N_i large enough such that for some small ϵ ,

$$\phi(\vec{r})/\phi_{\max} < \epsilon \quad (4.7)$$

for $|\vec{r}_i| > \Delta_i$. Here, one is actually choosing some finite cutoff on what is formally an infinite integral in the continuous Fourier transform.

In our computer simulations, we have experimented with detectors arranged in two planes as in Fig. 1 where the opening angle θ is such that $\tan (\theta/2) \cong 1$. We have found that for a given total number of lattice points, the reconstructions are best when the array dimension Δ_z (along the line perpendicular to the detector planes) is considerably larger than Δ_x and Δ_y . Such a result is reasonable since the scalar field ϕ from some finite density ρ falls most slowly in the direction of the detectors. In many cases it may be necessary to choose Δ_z to be larger than the distance between the detector planes.

It is possible to improve on a simple truncation by multiplying the field ϕ by an appropriate "window function" before computing the Fourier transform.

Window functions can reduce the leakage significantly, with the result that spurious oscillations in the solution ρ are significantly reduced. We have experimented with a variety of choices for the window function. In each case, the net effect is to make the cutoff in the Fourier transform relatively smooth. One example is known as the hanning function (11),

$$w(x) = 0.5 + 0.5 \cos (\pi x / \Delta_x) , \quad 0 \leq x \leq \Delta_x \quad (4.8)$$

$$w(x) = 0 \quad x < 0 \quad \text{and} \quad x > \Delta_x .$$

A second example, the hamming function (12), provides somewhat better results,

$$w(x) = 0.54 + 0.46 \cos (\pi x / \Delta_x) , \quad 0 \leq x \leq \Delta_x . \quad (4.9)$$

A third example, suggested by Blackman (13), yields even better results,

$$w(x) = 0.42 + 0.50 \cos (\pi x / \Delta_x) + 0.08 \cos (2\pi x / \Delta_x) \quad (4.10)$$

After some investigation, we have obtained the best results using window functions in the shape of a Gaussian (14)

$$w(x) = \exp \left[(x - \Delta_x / 2) / \alpha_x \right]^2 \quad (4.11)$$

with α_x in the range $0.25 \Delta_x$ to $0.40 \Delta_x$. The full window function in three dimensions must be,

$$W(\vec{r}) = w(x) w(y) w(z) \quad (4.12)$$

In our experience, the choice of window function makes a significant contribution to the quality of the reconstruction, and the Gaussian of Eq. (4.11) worked substantially better than the other examples mentioned.

V. Noise in the Data Leads to Unstable Solutions

In the ideal situation where the number of counts is infinite, the scalar field ϕ may be determined exactly. Then, the problem can be solved as illustrated in the previous sections, where the only limitation on accuracy is the computation time required by the size of the lattice. In the limit where the lattice extends to infinity and the lattice spacing shrinks to zero, the solution becomes exact.

However, the number of counts must be limited by both physical and medical considerations. The dose of radioisotope administered to the patient should be small enough to minimize adverse side effects and large enough to provide enough data for a reasonable reconstruction. In any case, there will be statistical variations in the measurement of the scalar field ϕ at the lattice sites.

If for a given dose to the patient, the positron camera is able to record N events after some reasonable exposure time, we can estimate the resolution limit of the reconstruction. Suppose the total number of sites in the lattice is M . Then each event will pass through approximately $M^{1/3}$ lattice sites and the number of events per lattice site is roughly $N/M^{2/3}$. To obtain statistical fluctuations less than some fraction ϵ , the following condition must be satisfied,

$$\frac{M^{1/3}}{N^{1/2}} \lesssim \epsilon \quad (5.1)$$

We have found that if an object has linear dimension A , reasonable reconstructions are obtained when the lattice size is roughly of linear dimension $3A$. The resolution δ is given simply by

$$\delta = 3A/M^{1/3} \quad (5.2)$$

and thus the resolution and the number of events are subject to an uncertainty relation

$$N^{1/2} \delta \gtrsim 3A/\epsilon \quad (5.3)$$

When the error ϵ grows to some (quite small) fraction, the reconstructions become unacceptable. For a given ϵ , the resolution may be improved in a well defined way by increasing N .

The largest acceptable level for ϵ depends strongly on the solid angle subtended by the detector. The effects of noise are coupled in a very nonlinear way to the solid angle limitations, as we shall show by studies described in a later paper. This results in very practical considerations for the detector configuration: The detector plates should be as large as possible, placed as close to the head as possible, and should surround the head on four sides rather than two. Engineering problems will be more than compensated by improved quality of the reconstruction.

Although the presence of noise is inevitable, a careful examination of the problem may minimize its effects, and even provide reasonable reconstructions where none was possible with a naive approach. The first step is to note that the convolution equation we must solve (3.1) is essentially a Fredholm equation of the first kind.

$$\phi(\vec{r}) = \int d^3 r' K(\vec{r}, \vec{r}') \rho(\vec{r}') \quad (5.4)$$

where the kernel $K(\vec{r}, \vec{r}')$ is given by the special form $\phi_0(\vec{r} - \vec{r}')$. The equation is nonsingular, since on a lattice, the integration limits are finite and the kernel is bounded.

It is well known that such an equation is unstable. This can be seen in the following way as described by Phillips (15). Suppose $\rho(\vec{r})$ is a solution to the equation (5.4). Consider a finite fluctuation in the solution, $\rho_m(\vec{r}) = \sin(mx)$. Then as $m \rightarrow \infty$,

$$\phi_m(\vec{r}) = \int d^3 r' K(\vec{r}, \vec{r}') \rho_m(\vec{r}') \rightarrow 0 \quad (5.5)$$

Hence, an infinitesimal fluctuation in the scalar field ϕ may produce a finite, nonvanishing fluctuation in the solution ρ . That is, the equation is unstable with respect to noise.

The instability of the equation places a limit on the resolution of the reconstruction. As the lattice distance is decreased, the accuracy of the reconstruction begins to improve, but at some point, the accuracy begins to worsen. The critical point occurs when the lattice spacing grows small enough to admit terms in the Fourier series with frequencies high enough for Eq. (5.5) to become valid.

The instability in Eq. (5.5) will occur for fairly small values of m if the kernel $K(\vec{r}, \vec{r}')$ is a smooth function of \vec{r}' . Conversely, the stability may be improved by choosing a kernel which is sharply peaked. In the extreme case in which the kernel is a delta function, $K(\vec{r}, \vec{r}') = \delta(\vec{r} - \vec{r}')$, there is no instability.

In Section II, we discussed various possibilities for the kernel (or Green's function) in the convolution integral. In the absence of noise, all the choices are equally valid. However, in the presence of noise, it is clear that greater stability for the solution can be achieved by choosing a scalar field with sharp peaks. Such peaks occur in the scalar fields discussed in Example C in Section II. If the detector consists of two parallel plates, orient the coordinate system such that the z -axis is perpendicular to the plates. Then the scalar field will be peaked for large negative values of n . That is, events near the edges of the universal cone are given the greatest weight. (Large positive values of n produce a sharply peaked kernel in the x and y directions, but not in the z direction, thus degrading resolution in the z direction. In fact, as $n \rightarrow \infty$, we are left with a simple two dimensional projection down the z -axis.)

At first it may appear that as n is made more and more negative, the solutions will become more and more stable. However, there is a second balancing effect. As n becomes more negative, the cone of detection becomes effectively more restricted, and less of the data is used for the reconstruction. Events with small θ are given less weight, and there is some point at which the reconstruction must begin to suffer. We have found that the choice $n=-3$ seems to yield the best reconstructions. The quality of the reconstructions is not a strong function of the choice for n . For example, $n=-2$, -4 , -5 seem to work about as well as $n=-3$.

VI. Noise Instabilities May Be Removed

Phillips (15) has suggested a technique for dealing with the problem of noise which removes the instability in the equation (5.4). His discussion applies to any nonsingular Fredholm equation of the first kind, and therefore may be applied to our problem. However, we shall recast his treatment, since the convolution integral permits a particularly elegant realization of the technique. In particular, it will be convenient to work in three dimensions and in the continuum rather than on a lattice.

Suppose the scalar field $\phi(\vec{r})$ is known only up to some error $\epsilon(\vec{r})$. Then, the equation to be solved is,

$$\phi(\vec{r}) + \epsilon(\vec{r}) = \int d^3 r' \phi_0(\vec{r} - \vec{r}') \rho(\vec{r}') \quad (6.1)$$

where the error $\epsilon(\vec{r})$ is an arbitrary function except for some condition on its magnitude, such as $|\epsilon(\vec{r})| \leq M$. Equation (6.1) may be solved for $\rho(\vec{r})$ by taking the Fourier transform, as outlined in Section III,

$$\rho(\vec{r}) = \int d^3 r' [\epsilon(\vec{r}') + \phi(\vec{r}')] \int d^3 p \frac{\exp[-2\pi i \vec{p} \cdot (\vec{r} - \vec{r}')] }{\Phi_0(\vec{p})} \quad (6.2)$$

The functional derivative of $\rho(\vec{r})$ with respect to $\epsilon(\vec{r}')$ is a function of $\vec{r} - \vec{r}'$,

$$\frac{\delta \rho(\vec{r})}{\delta \epsilon(\vec{r}')} = \int d^3 p \frac{\exp[-2\pi i \vec{p} \cdot (\vec{r} - \vec{r}')] }{\Phi_0(\vec{p})} \equiv \alpha(\vec{r} - \vec{r}') \quad (6.3)$$

The error tends to be random from point to point, and it generates instabilities in the solution $\rho(\vec{r})$ which are manifested as sharp fluctuations. Thus, a reasonable condition on $\rho(\vec{r})$ is a requirement for smoothness, in which a solution is sought such that

$$\int d^3 r \left[\nabla^2 \rho(\vec{r}) \right]^2$$

is minimized.

Suppose the total error is some fixed number e where

$$e^2 = \int d^3 r [\epsilon(\vec{r})]^2 \quad (6.4)$$

Then the smoothness condition may be re-expressed by introducing a Lagrange multiplier $1/\gamma$ and minimizing the following expression with respect to variations in $\epsilon(\vec{r})$:

$$\int d^3 r \left[\nabla^2 \rho(\vec{r}) \right]^2 + \frac{1}{\gamma} \int d^3 r \epsilon(\vec{r})^2$$

It is clear that γ must be nonnegative, if there is to be a meaningful solution.

The functional derivative of this expression with respect to $\epsilon(\vec{r}')$ gives an expression for the smoothness condition on the solution $\rho(\vec{r})$,

$$0 = \gamma \int d^3 r \nabla^2 \rho(\vec{r}) \cdot \nabla^2 \frac{\delta \rho(\vec{r})}{\delta \epsilon(\vec{r}')} + \epsilon(\vec{r}') \quad (6.5)$$

subject to the constraint, Eq. (6.4).

Integration by parts and use of Eq. (6.3) yields an expression for the error which is proportional to γ ,

$$\epsilon(\vec{r}') = -\gamma \int d^3 r' \rho(\vec{r}') \nabla'^4 \alpha(\vec{r}' - \vec{r}) \quad (6.6)$$

where

$$\nabla'^4 \alpha(\vec{r}'-\vec{r}) = (2\pi)^4 \int d^3 p \frac{p^4}{\Phi_0(\vec{p})} \exp[-2\pi i \vec{p} \cdot (\vec{r}'-\vec{r})] \quad (6.7)$$

Substituting Eq. (6.6) into Eq. (6.1) gives a new convolution equation,

$$\int d^3 r' \left[\phi_0(\vec{r}-\vec{r}') + \gamma \nabla'^4(\vec{r}'-\vec{r}) \right] \rho(\vec{r}') = \phi(\vec{r}) \quad (6.8)$$

The solution for the density distribution in momentum space is simply

$$R(\vec{p}) = \frac{\Phi(\vec{p})}{\Phi_0(\vec{p}) + \gamma \frac{(2\pi)^4 p^4}{\Phi_0(\vec{p})}} \quad (6.9)$$

while the error is expressed in terms of the Lagrange multiplier

$$\epsilon(\vec{r}) = -\gamma (2\pi)^4 \int d^3 p \exp(-2\pi i \vec{p} \cdot \vec{r}) \frac{p^4 R(\vec{p})}{\Phi_0(\vec{p})} \quad (6.10)$$

The ideal case in which there is no error in the determination of the scalar field corresponds to setting $\gamma=0$. Then Eq. (6.9) reduces to the canonical solution of the convolution equation given in Eq. (3.4). Increasing the value of γ increases the amount of smoothing in the solution $\rho(\vec{r})$.

In the case where there is a finite error, an estimate for the appropriate value for γ may be obtained iteratively. First choose some small value for γ and compute $R(\vec{p})$. Then using Eq. (6.10) compute the corresponding error function and compare the result to the total error e expected from statistical fluctuations in the data. Only a few iterations are needed, since by Eq. (6.10), the total error e is roughly proportional to γ .

From the form of the solution in Eq. (6.9), it can be seen that the incorporation of this technique into the mathematical analysis is rather simple and

straightforward. No extra Fourier transforms or scalar fields need to be computed for Eq. (6.9). All that is needed is a simple recombination of the scalar field ϕ_0 .

We have found that the use of this technique is the single most important factor in improving the quality of our reconstructions.

VII. The Algorithm is Summarized

A. From the configuration of the detectors and the dimensions of the region to be imaged, compute the universal cone of detection.

B. Choose the lattice spacings, δ_x , δ_y , δ_z , taking into account the desired resolution, aliasing, detector configuration, and noise in the data.

C. Choose the array dimensions, $\Delta_i = N_i \delta_i$, to be large enough to make leakage unimportant.

D. Compute the scalar field from a point emitter, $\phi_0(\vec{r})$, choosing the form which minimizes instabilities in the solution. E.g., take $n=-3$ in the definition for ϕ_0 in Eq. (2.6).

E. Choose a window function, $W(\vec{r}) = w(x) w(y) w(z)$, which minimizes leakage. E.g., take $w(x)$ to be a Gaussian as in Eq. (4.11).

F. Compute the Fourier transform of $\phi_0(\vec{r}) W(\vec{r})$, which we shall denote as $\Phi_0(\vec{p})$. (All the steps up to this point need be performed only once for a given positron camera, with $\Phi_0(\vec{p})$ stored on a tape.)

G. Using the data collected by the camera, compute the scalar field $\phi(\vec{r})$ due to the density distribution using the same definition employed in step D. Only data falling inside the universal cone are used.

H. Compute the Fourier transform of $\phi(\vec{r}) W(\vec{r})$ which we shall denote as $\Phi(\vec{p})$.

I. Compute the solution in momentum space,

$$R(\vec{p}) = \frac{\Phi(\vec{p}) \exp(2\pi i \vec{p} \cdot \vec{a})}{\Phi_0(\vec{p}) + \gamma (2\pi)^4 p^4 / \Phi_0(\vec{p})} \quad (7.1)$$

where the parameter γ is determined by the estimated level of noise in the data. (See Section VI.) The point \vec{a} is the central point in the lattice array, and the phase shift is necessary since the functions are defined on a lattice where $\vec{r}=\vec{0}$ is located at a corner and $\vec{r}=\vec{a}$ is located in center of the array.

J. Compute the inverse Fourier transform of $R(\vec{p})$, and finally obtain the reconstruction of the radioisotope density, $\rho(\vec{r})$.

VIII. The Computer Solutions are Feasible

In this section we shall discuss the results obtained by applying our algorithm to a computer generated phantom. For convenience, we have chosen a relatively modest lattice of dimensions 32 by 32 by 32 to illustrate our results. In principle, a somewhat larger lattice can be chosen to obtain better resolution, if one is willing to pay for the extra computation time.

The Fourier transforms are performed using a Fast Fourier Transform program written by Singleton (16), and the actual computing was done on a CDC 7600 at the Lawrence Berkeley Laboratory. Two Fourier transforms are required for a reconstruction, and we found that for our lattice dimensions, the time required was 2.5 seconds per transform. In general, the time required for a lattice with M sites is roughly proportional to $M \log_4 M$, so the time required for larger lattices may be estimated from our results.

For a given detector configuration, the scalar field for a point emitter $\phi_0(\vec{r})$ and its Fourier transform $\Phi_0(\vec{p})$ need be computed only once and then stored. Reconstructions for arbitrary objects can then be made using the stored values

for $\Phi_0(\vec{p})$. Therefore, there is no need to economize on time spent in computing $\Phi_0(\vec{p})$. We have found that the quality of the reconstructions depends strongly on the accuracy with which $\phi_0(\vec{r})$ and $\Phi_0(\vec{p})$ are computed. In particular, for a detector configuration of limited solid angle, the scalar field $\phi_0(\vec{r})$ has large variations near the origin and effects at the edge of the universal cone are important there. Since time spent computing $\Phi_0(\vec{p})$ is rather unimportant, there is a great advantage to doing it with great care.

We have generated a set of data in the computer by Monte Carlo corresponding to a phantom, consisting of a "skull region" corresponding to the blood supply for the brain, a "brain", and a hypothetical "tumor." The "skull region" was a spherical shell 3 cm thick, with an inner radius of 18 cm and an outer radius of 21 cm, and with a relative radioisotope density, $\rho=1.0$. The "brain" was located inside the skull, with density $\rho=0.2$. The "tumor" was a sphere located off-center in the "brain," with a radius of 3.6 cm and a density $\rho=2.0$. The relative radioisotope densities are similar to those found in actual patients (17). The phantom was permitted to generate a total of 818,785 positron emissions.

We chose a detector configuration of two parallel square plates. Relatively modest increases in the size of the plates were capable of producing significant improvement in the quality of the reconstructions. Alternatively, if the head is surrounded on four sides with detectors, there would be an even more marked improvement, while only doubling the detector area.

In this paper we shall show our results for a detector where the plates are 84.86 cm by 84.86 cm and 50 cm apart. For such a configuration, 229,429 of the total events generated were detected by the camera.

The lattice distances were 2.5 cm by 2.5 cm by 5.0 cm, thus making the array dimensions 80 cm by 80 cm by 160 cm. We found it necessary to make the array considerably larger in the z-direction to optimize the reconstructions. Gaussian window functions were used, and we found that the best values for the parameters α_i in Eq. (4.11) were 32 cm, 32 cm, and 40 cm. The scalar field was defined as in Eq. (2.6) with $n=-3$.

In Fig. 5 we show the results of our reconstruction for two different values of the parameter γ . In each case, only the central plane, passing through the center of the tumor is shown. The numbers indicate relative densities, where zero is indicated by a blank space. Figure 6a corresponds to the application of our algorithm with $\gamma=0$, where no noise filter is used. It is clear that noise in the data is important enough to create such large instabilities that the reconstruction is useless. In fact, there are large regions in which the densities are negative. Figure 6b shows the results for $\gamma=2 \times 10^{-6}$. The improvement is dramatic, and the reconstruction is a reasonable facsimile of the actual density. Negative densities still appear, but they are relatively insignificant.

In Figs. 6, 7, and 8, we show reconstructions displayed on a cathode ray tube, using a program which can differentiate 64 gray levels in the display (18). The density of dots is proportional to the density in the reconstruction. In each figure, we have shown a series of planes in the reconstruction, starting from the central plane and working outward in one direction.

Figure 6 shows the actual density distribution being used to generate the data. This gives the reader a basis of comparison for the quality of the reconstructions.

Figure 7 shows the results obtained by a simple back projection of the data, as described in Section I. Only those events lying inside the universal cone are

used, to remove any bias as one moves out toward the edges. The tumor is clearly visible in the central plane, but the contrast has been severely degraded by shadows from other planes. Furthermore, the tumor has cast a recognizable shadow on at least two other planes, where it does not exist.

Figure 8 shows the results obtained using our algorithm. Here we have set $\gamma = 5 \times 10^{-5}$ which seems to give the best reconstructions. Computing with Eqs. (6.4) and (6.10), we find the corresponding value for the root mean squared deviation to be $e = 237$. One may estimate e corresponding to the statistical fluctuations to be 2461. Thus the optimal value for γ appears to be smaller than would have been expected, a phenomenon also observed by Phillips. The image of the tumor appears quite clearly, and shadowing onto other planes has disappeared. The improvement over the back projection is obvious. And comparison with the actual density is very favorable.

IX. Compton Scattering May Be Dealt With

So far we have not mentioned experimental sources of background other than statistical fluctuations in the data. It has been found that a serious source of background arises from the possibility that a photon may undergo Compton scattering before emerging from the patient's body (19). A second source arises from the possibility that a photon may fail to trigger a response at the point where it enters the detector, undergo Compton scattering inside the detector, and finally trigger a response at some other point (19). We believe that both problems may be solved rather simply in the context of our algorithm.

The Green's function for Compton scattering inside the patient is generally a function of position. However, consider a roughly spherical region like the head. If the point of annihilation occurs at the center of the head, both photons will traverse equal paths before emerging, with the sum of path lengths equal to

the diameter of the head. If annihilation occurs toward the edge of the head, the path lengths of the two photons will be different, but the sum will still be roughly the diameter of the head. Thus the probability for Compton scattering will be the same in both cases.

Expressing this quantitatively, we assume that the two photons must travel distances x_1 and x_2 , respectively, in the head, while the distance $d = x_1 + x_2$ is a fixed number independent of the annihilation point. Suppose that the effective attenuation coefficient for head tissue is given by a fixed number μ . (The probability that a photon pass through tissue of thickness x is given by $P = e^{-\mu x}$.) Then the probability that both of the photons will emerge from the head without scattering or absorption is

$$P_1 P_2 = e^{-\mu x_1} e^{-\mu x_2} = e^{-\mu d} ,$$

independent of the position of annihilation. The probability that either photon undergo Compton scattering is therefore proportional to

$$1 - e^{-\mu d} ,$$

also independent of position.

Of course, the attenuation coefficient is significantly different in bone than in soft tissue and thus not a fixed number. However, almost all annihilation events will occur inside the skull, and both photons will have to pass through the skull before emerging, again leaving the probability for scattering roughly independent of position.

We conjecture that the Green's function will prove to be roughly independent of position in the head, when measured experimentally.

Similarly, if the detectors give a uniform response over their entire surface area, then the Green's function for false triggering in the detector will also be independent of position. Edge effects may be removed by sufficient restriction of the universal cone.

We are then left with the familiar convolution in Eq. (3.1) except that now the Green's function $\phi_0(\vec{r})$ is the scalar field due to a point emitter in a patient's head, as measured by a real detector. The subsequent algorithm is identical. The only difference is that the scalar field $\phi_0(\vec{r})$ must be measured experimentally rather than calculated for the ideal case.

(We shall reserve explicit investigation of Compton scattering for a future paper.)

We therefore conclude that Fourier techniques afford an extremely attractive means of obtaining three dimensional reconstructions with the positron camera. Experimental problems such as limited detector configuration, statistical fluctuations in the data, Compton scattering within the patient, and false detector response may all be treated by a technique in a natural and elegant manner. The method appears to be simple, feasible, and practical.

Many questions await investigation: how various detector configurations affect the quality of the reconstruction; whether there are more effective means for dealing with noise in the data; if iterative schemes utilizing all the data obtained by the camera are feasible; whether convolution methods instead of Fourier transforms are more efficient. There may be room for great improvement in obtaining reconstructions in the positron camera.

Acknowledgments

We wish to thank Victor Perez-Mendez for suggesting this problem to us and for his advice and enthusiasm during the course of our work. We extend our thanks to Paul Concus for a very important discussion concerning the problem of noise, to Burns Macdonald for generously making programs for the Fast Fourier Transform and the CRT displays available, to Dennis Chu, C. B. Lim and Victor Perez-Mendez for discussions concerning the experimental problems, and to Oscar Buneman, Ron Bracewell, Loren Meissner, and Ron Huesman for discussions of mathematical problems. One of us (G.C.) thanks J. D. Jackson of the Theoretical Physics Group at LBL and Sid Drell of the Theoretical Physics Group at SLAC for their support and encouragement while much of this work was being done.

References

1. Wallace PR: Positron Annihilation in Solids and Liquids. Solid State Physics 10: Seitz FR and Turnbull D, editors, New York, Academic Press, 1960, p. 24.
2. Anger HO: Radioisotope Cameras. Instrumentation in Nuclear Medicine. Hine GJ, editor, New York, Academic Press, 1967, pp 485-552.
3. Burnham CA and Brownell GL: A Multicrystal Positron Camera. IEEE Transactions in Nuc. Sci. NS-19, No. 3: 201-205, 1972.
4. Muehllehner G: Positron Camera with Extended Counting Rate Capability. J. Nuc. Med. 16: 653-657, 1975.
5. Lim CB, Chu D, Perez-Mendez V, Kaufman L, Hattner RS, Price DC: Initial Characterization of a Multiwire Proportional Chamber Positron Camera. IEEE Transactions in Nuc. Sci. NS-22, No. 1: 388-394, 1975.
6. Hattner RS, Lim CB, Swann SJ, Kaufman L, Perez-Mendez V, Chu D, Huberty JP, Price DC, Wilson CB: Cerebral Imaging Using ^{68}Ga DTPA and the U. C. S. F. Multiwire Proportional Chamber Positron Camera. Presented at IEEE Meeting, San Francisco, November 1975, to be published in IEEE Transactions in Nuc. Sci., February 1976.
7. Zaklad H, Derenzo S, Muller RA, Smadja G, Smits RG, Alvarez LW: A Liquid Xenon Radioisotope Camera. IEEE Transactions in Nuc. Sci. NS-19: 201, 1972.
8. For a review of the techniques, see Gordon R and Herman GT: Three Dimensional Reconstruction from Projections: A Review of Algorithms. International Review of Cytology 38: Bourne GH and Danielli JF, editors, New York, Academic Press, 1974, pp 111-154; Cho ZH (editor): Special

Issue on Physical and Computational Aspects of 3D Image Reconstruction.

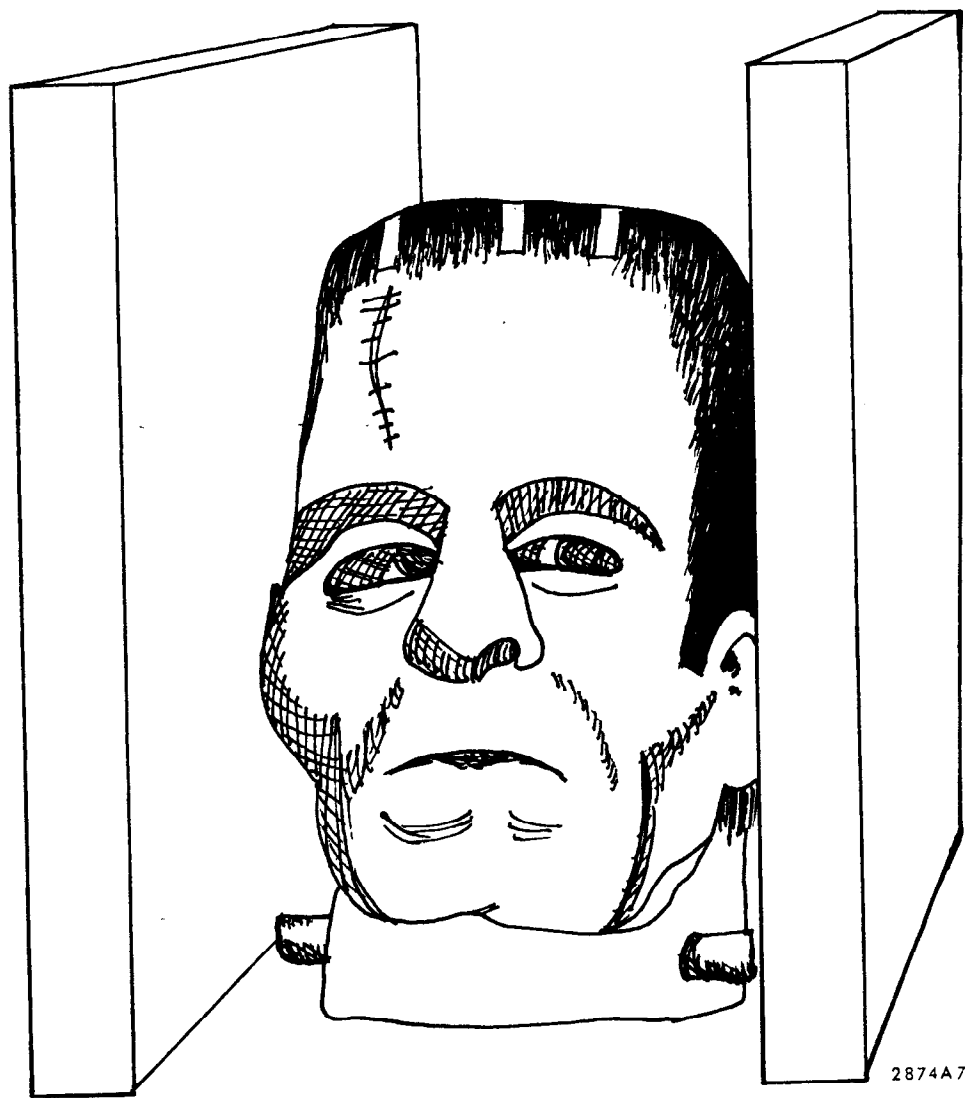
IEEE Transactions on Nuc. Sci. NS-21, No. 3: 1-96, 1974.

9. Chu G: An Algorithm for Three Dimensional Resolution in the Positron Camera, unpublished LBL memorandum, May 1975.
10. For a concise account of the problems and techniques for discrete Fourier transforms, see Brigham O: The Fast Fourier Transform. New York, Prentice Hall, 1974.
11. This is named for the Austrian meteorologist, Julius von Hann; see Blackman RB and Tukey JW: The Measurement of Power Spectra from the Point of View of Communications Engineering. New York, Dover, 1958, p 98.
12. Hamming RW and Tukey JW: Measuring Noise Color, unpublished memorandum, and Blackman RB and Tukey JW. op. cit., p 98.
13. Blackman RB and Tukey JW: op. cit., p 98.
14. This window function was suggested to us by Ron Bracewell and by Oscar Buneman.
15. Phillips DL: A Technique for the Numerical Solution of Certain Integral Equations of the First Kind. J. Assoc. of Computing Machinery 9: 84-97, 1962. We express sincere thanks to Paul Concus for calling this paper to our attention.
16. Singleton RC: An Algorithm for Computing the Mixed Radix Fast Fourier Transform. IEEE Transactions on Audio and Electroacoustics AU-17: 93-103, 1969.
17. Chu D: private communication.
18. We thank Burns Macdonald for kindly making this display program available.
19. Chu D and Lim CB: private communication.

Figure Captions

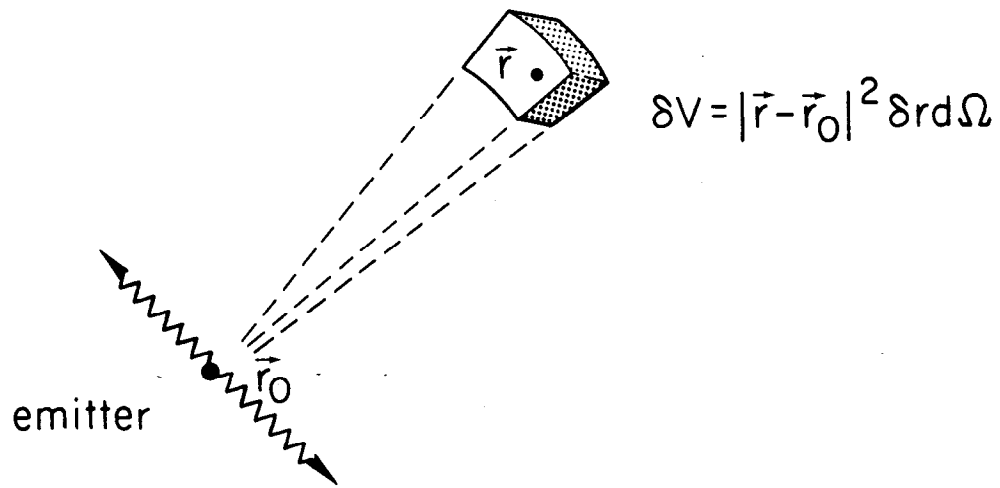
1. Schematic diagram of a possible detector configuration in which the camera is used to image the radioisotope distribution in a hypothetical head phantom.
2. a) Volume element, subtending a solid angle $\delta\Omega$, with thickness δr , located at a distance $|\vec{r}-\vec{r}_0|$ from the point emitter: the wiggly lines indicate two back-to-back photons. b) Volume element, of radius δr , located at the site of the point emitter.
3. Area element with sides of length a , located at a distance $|\vec{r}-\vec{r}_0|$ from the point emitter, oriented perpendicular to the z-axis, at an angle θ with respect to the z-axis: the wiggly lines indicate two back-to-back photons.
4. Two dimensional schematic illustration of an oval head phantom placed between two parallel detector plates: at the point \vec{r}_2 , we have drawn both the universal cone of detection (shaded, with opening angle θ) and the local cone of detection (unshaded, and containing the universal cone); at the point \vec{r}_1 , the universal and local cones happen to be identical with the common opening angle θ .
5. Reconstruction of the computer generated phantom with noise for two different values of the parameter γ (only the central plane perpendicular to the z-axis passing through the center of the tumor is shown): (a) $\gamma=0$, where no noise filter is used and the instability has left no trace of the phantom; (b) $\gamma=2 \times 10^{-6}$, where the tumor and skull region are now visible.
6. Actual noise free density distribution used to generate the phantom by Monte Carlo: (a) shows the central plane passing through the center of the tumor; (b), (c), (d), (e), (f) show parallel planes, each successively displaced from the central plane by 5 cm; the "skull region" is 3 cm thick, with inner radius of 18 cm, and relative radioisotope density $\rho=1.0$; the "brain" has density $\rho=0.2$; the "tumor" has a radius of 3.6 cm and density $\rho=2.0$.

7. Reconstruction of the phantom with noise by back projection: the planes in (a) through (f) correspond to those in Fig. 6.
8. Reconstruction of the phantom with noise by Fourier techniques setting $\gamma = 5 \times 10^{-5}$ to optimize the quality: the planes in (a) through (f) correspond to those in Fig. 6; negative densities were insignificant and have been set equal to zero; the results are a marked improvement over the back projection in Fig. 7.

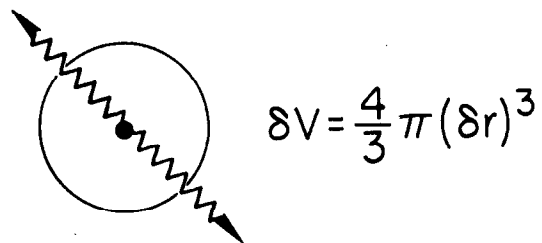


2874A7

Fig. 1



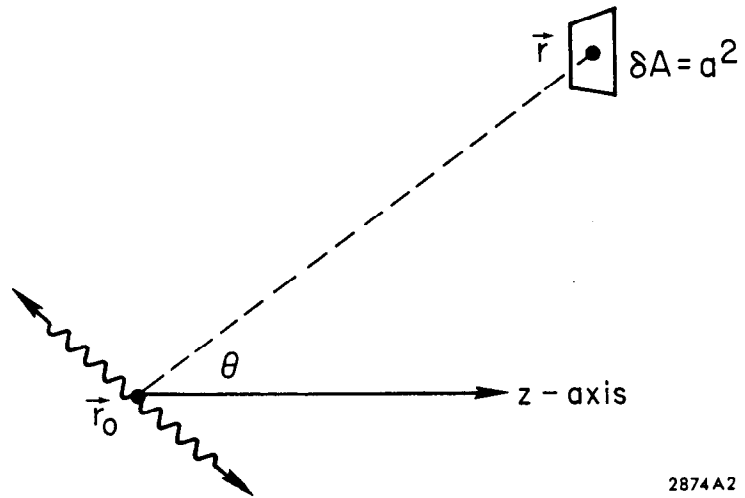
(a)



(b)

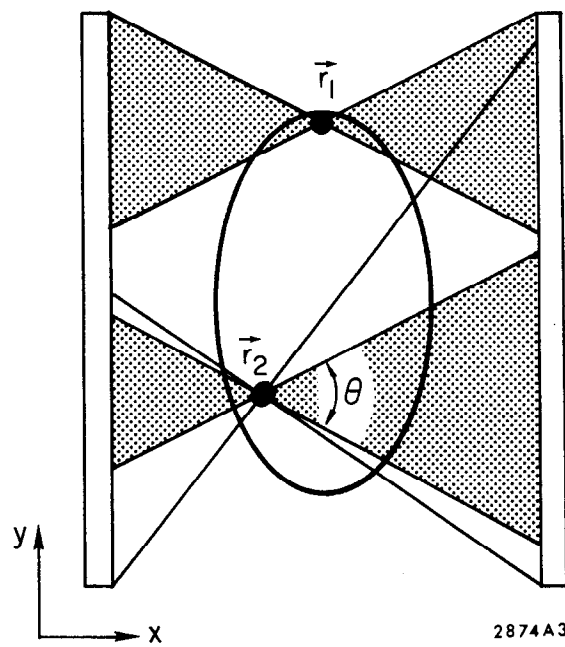
2874A1

Fig. 2



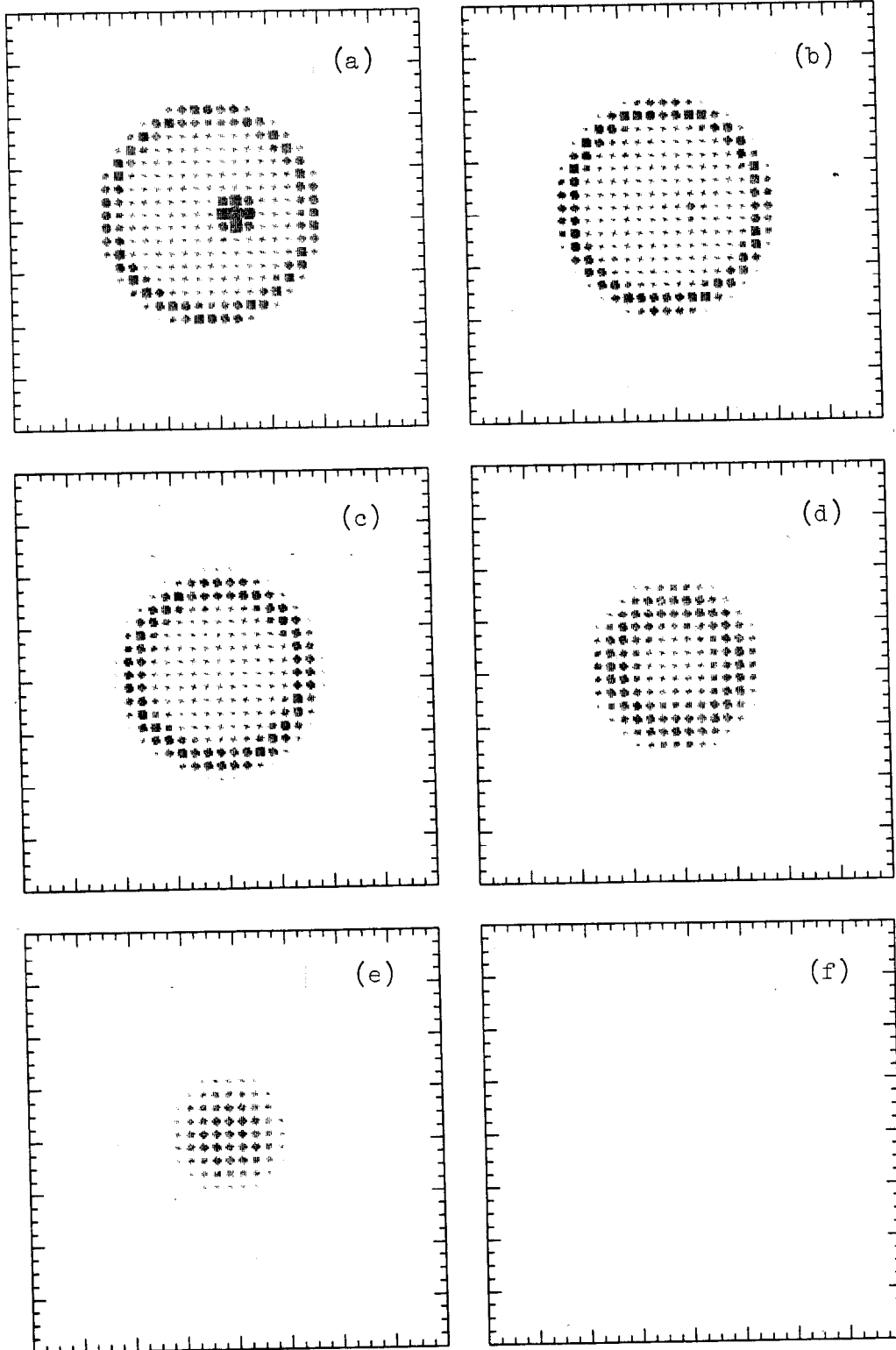
2874A2

Fig. 3



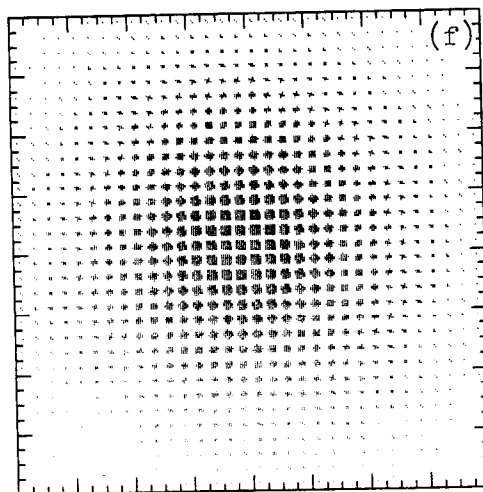
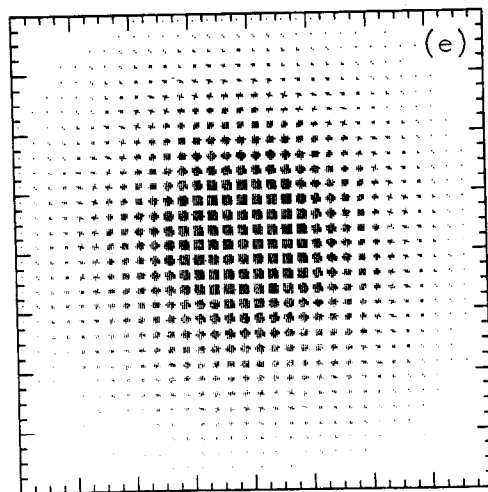
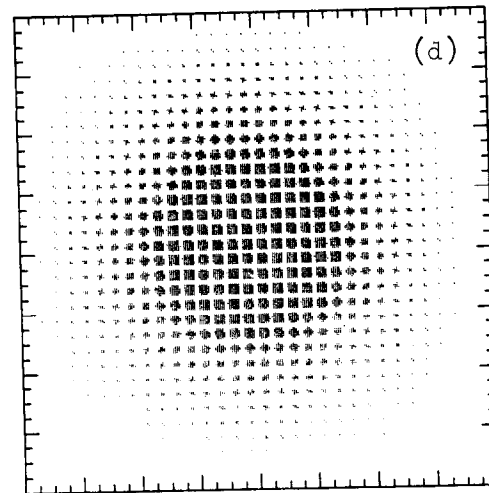
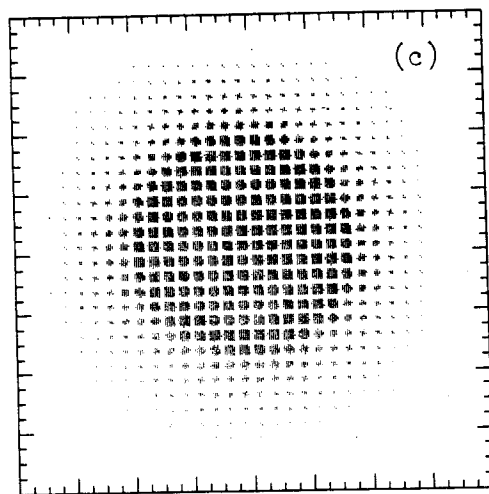
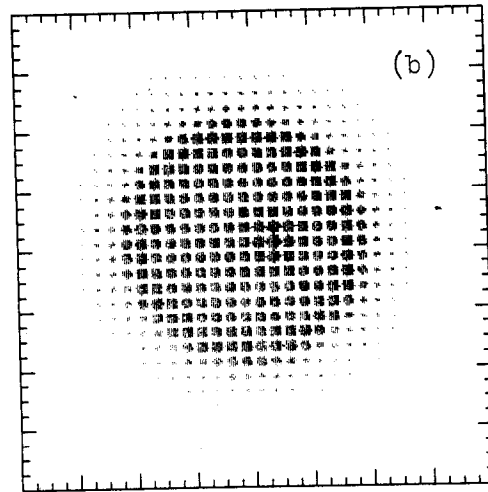
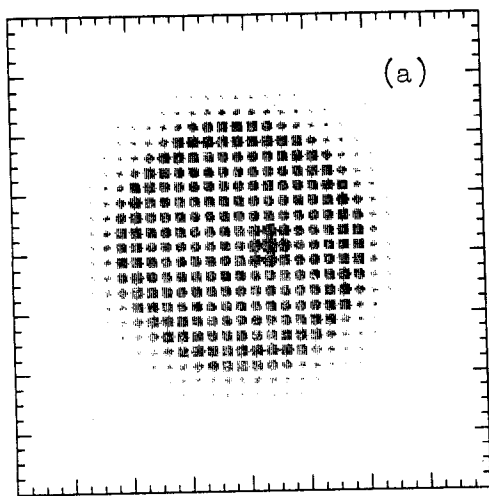
2874A3

Fig. 4



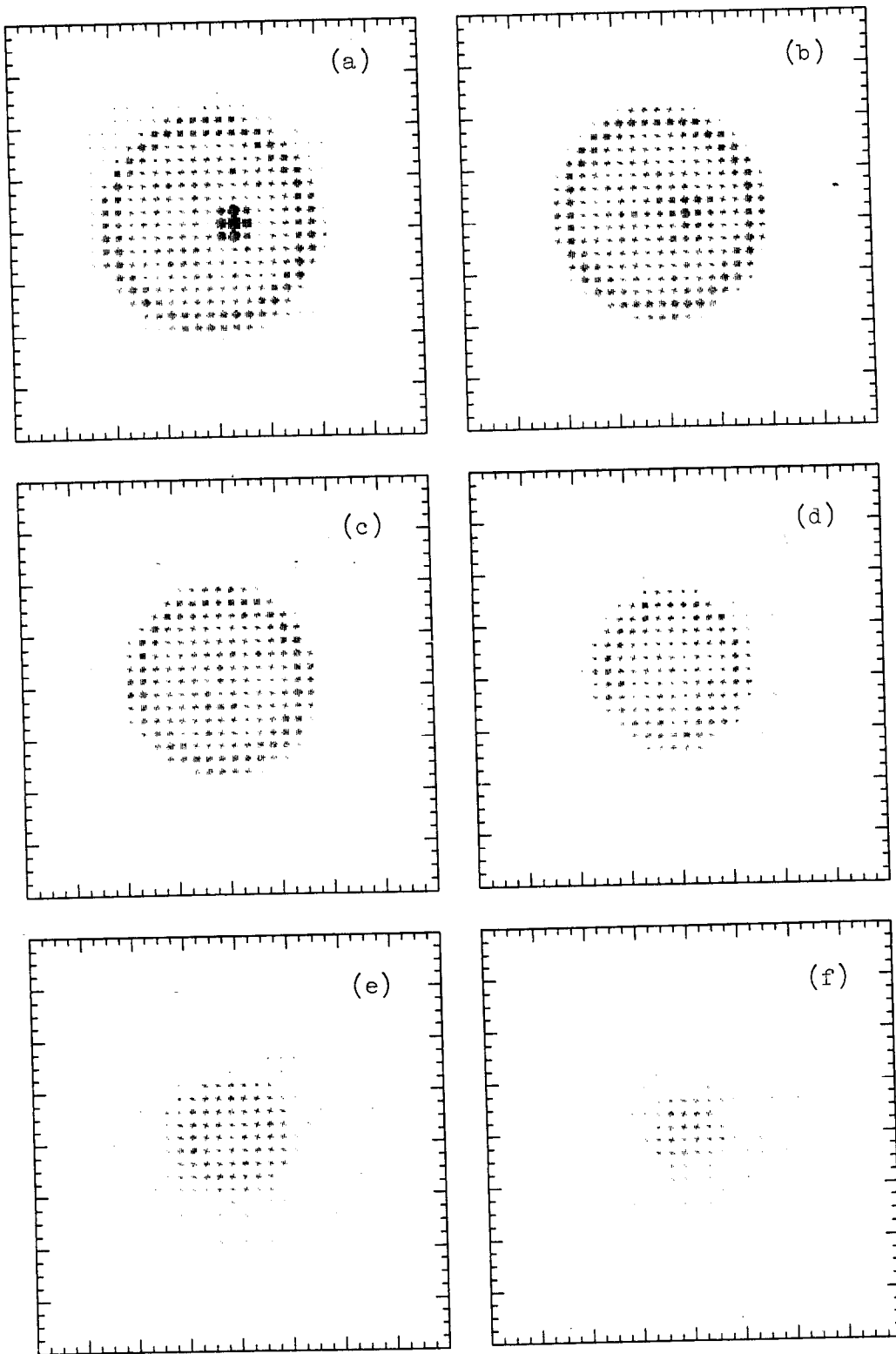
2874A4

Fig. 6



2874A6

Fig. 7



2874A5

Fig. 8